AGU PUBLICATIONS

Journal of Advances in Modeling Earth Systems

RESEARCH ARTICLE
10.1002/2017MS000991

Parameterization Interactions in Global Aquaplanet Simulations

Ritthik Bhattacharya[1], Simona Bordoni[1], Kay Suselj[2], and João Teixeira[2]

[1]California Institute of Technology, Pasadena, California, USA, [2]Jet Propulsion Laboratory, California Institute of Technology, Pasadena, California, USA

Key Points:
- To understand parameterization interactions in a GCM, aquaplanet simulations are performed in WRF using a suite of convection/BL schemes
- While the generated mean climates have qualitative similarities, differences are seen in cloud and precipitation behavior (amount & types)
- These differences arise from how the BL scheme interacts with convection, both directly and via large-scale dynamics and microphysics

Correspondence to:
R. Bhattacharya,
ritthikiit@gmail.com

Citation:
Bhattacharya, R., Bordoni, S., Suselj, K., & Teixeira, J. (2018). Parameterization interactions in global aquaplanet simulations. *Journal of Advances in Modeling Earth Systems*, *10*, 403–420. https://doi.org/10.1002/2017MS000991

Received 12 APR 2017
Accepted 10 JAN 2018
Accepted article online 18 JAN 2018
Published online 9 FEB 2018

Abstract Global climate simulations rely on parameterizations of physical processes that have scales smaller than the resolved ones. In the atmosphere, these parameterizations represent moist convection, boundary layer turbulence and convection, cloud microphysics, longwave and shortwave radiation, and the interaction with the land and ocean surface. These parameterizations can generate different climates involving a wide range of interactions among parameterizations and between the parameterizations and the resolved dynamics. To gain a simplified understanding of a subset of these interactions, we perform aquaplanet simulations with the global version of the Weather Research and Forecasting (WRF) model employing a range (in terms of properties) of moist convection and boundary layer (BL) parameterizations. Significant differences are noted in the simulated precipitation amounts, its partitioning between convective and large-scale precipitation, as well as in the radiative impacts. These differences arise from the way the subcloud physics interacts with convection, both directly and through various pathways involving the large-scale dynamics and the boundary layer, convection, and clouds. A detailed analysis of the profiles of the different tendencies (from the different physical processes) for both potential temperature and water vapor is performed. While different combinations of convection and boundary layer parameterizations can lead to different climates, a key conclusion of this study is that similar climates can be simulated with model versions that are different in terms of the partitioning of the tendencies: the vertically distributed energy and water balances in the tropics can be obtained with significantly different profiles of large-scale, convection, and cloud microphysics tendencies.

1. Introduction

In global climate models (GCMs), physical processes with scales smaller than the size of the numerical grid are not resolved by the large-scale discretized equations and hence need to be parameterized to represent their impact on the resolved grid-scale motions. In particular, boundary layer and moist convection mixing are traditionally parameterized separately even though it is understood that they are tightly entangled (Raymond, 1995). Here we investigate how different boundary layer and convection parameterizations interact with each other in a global model and how they produce different mean-state climates. As suggested by a number of recent studies (Cesana et al., 2017; Medeiros et al., 2008, 2015, 2016; Stevens & Bony, 2013), aquaplanet simulations provide an attractive framework for these investigations, as they retain the dynamics and physics of fully realistic simulations, but eliminate complexities arising from land surface, topography, and other zonal asymmetries. In addition, lack of long timescale processes associated with the ocean circulation and land implies that a shorter spin-up is required to reach equilibrium of the generated climate (Williamson et al., 2012), making it computationally more feasible to perform numerous simulations.

We use the global version of the Weather Research and Forecast model (WRF ARW V3; Skamarock et al., 2008) for our experiments. WRF provides a suite of several different options for the physical parameterizations that is ideal for our goals. In addition to the standard parameterizations available in the public WRF release, we implement a variation of the Eddy-Diffusivity Mass-Flux (EDMF) scheme (Suselj et al., 2012, 2013, 2014) as a unified boundary layer (BL) and shallow convection parameterization. The EDMF has different underlying assumptions compared to traditional diffusivity schemes (Siebesma et al., 2007) like the default Mellor Yamada Nakanishi Niino (MYNN) scheme (Nakanishi & Niino, 2006) in WRF. Unlike the MYNN, which models turbulence with a down-gradient transport, the EDMF scheme also includes representation of the

nonlocal transport. Here we want to explore how the interactions between this scheme and other parameterizations and the mean flow influence the simulated mean climate.

With these aims in mind, this paper is organized as follows: in section 2, we provide a brief overview of the model configuration and the suite of parameterizations used in our simulations. The mean climates generated by different parameterization combinations are described in section 3. Differences among these simulations are discussed in section 4, with a specific emphasis on the interaction between the convection and boundary layer schemes. Concluding remarks follow in section 5.

2. WRF in Aquaplanet Configuration

2.1. Setup

We perform simulations using the global WRF model (ARW, Version 3) (Skamarock et al., 2008) in aquaplanet setup (Hoskins et al., 1999). This setup has also been utilized in Bhattacharya et al. (2017), as well as in Cesana et al. (2017). The horizontal resolution is $1^\circ \times 1^\circ$ and we use a stretched vertical mesh with 40 levels up to the top of the atmosphere. The experiments are similar to the ones in the AquaPlanet Intercomparison Project (APE) archive (Medeiros et al., 2008; Williamson et al., 2012). The prescribed sea surface temperature (SST) is held constant and varies only with latitude (zonal symmetry). The SST distribution used here is the same as in experiment B in Medeiros et al. (2008), which is also called experiment QOBS in the APE archive. The prescribed insolation is held at its constant equinox distribution, that is, there is no seasonal cycle. Six simulations are performed using widely varying BL schemes (EDMF and MYNN, described below) for a range of modeled convective activity starting from no cumulus scheme to moderate (Tiedtke scheme) to highly active (GFS scheme) (Bhattacharya et al., 2017). Dudhia et al. (2012) and Biswas et al. (2014) show that the Tiedtke and GFS (simplified Arakawa Schubert scheme designed for the Global Forecasting System of the National Centers for Environmental Prediction (Han & Pan, 2011)) lie at opposite extremes in terms of the ratio of convective to stratiform precipitation in WRF, with the former and the latter having the smallest and largest ratio, respectively (and other convection schemes lying in between). Consequently, they also lie at opposite extremes in the range of convective heating profiles. Our motivation for employing these widely varying convection and boundary layer schemes is to explore how these schemes interact in a global model to generate different mean climates. A brief description of the used parameterizations is provided below.

2.2. Boundary Layer Scheme

2.2.1. Eddy-Diffusivity

The eddy-diffusivity (ED) parameterization follows the MYNN scheme (Nakanishi & Niino, 2006). The scheme is of order 2.5, i.e., the turbulence kinetic energy (TKE) is solved prognostically while the vertical turbulent fluxes (fluxes of momentum, heat, and other scalars) are solved diagnostically using the TKE and a diagnostic length scale. LES data are used to determine the functional form of the length scale and to help constrain the impact of different stability functions on that length scale (impact of atmospheric stability on the eddy size) (Nakanishi & Niino, 2006).

2.2.2. Eddy-Diffusivity Mass-Flux

The eddy-diffusivity mass-flux (EDMF) parameterization (Suselj et al., 2013) computes the vertical turbulent and convective fluxes as the sum of an eddy-diffusivity and a mass-flux contribution. The idea behind this approach is to decompose turbulence into a small-scale part driven by local gradients (modeled using eddy-diffusivity) and a larger-scale (yet subgrid to the resolved scale) part driven by convective plumes (represented by a mass-flux component). The mass-flux component models updrafts that originate at the surface and transport heat, moisture, and momentum vertically. Upon reaching condensation these updrafts continue as moist updrafts until they dissipate. The updrafts interact with their environment stochastically. In addition to small-scale turbulence, which is modeled by the eddy-diffusivity schemes, the EDMF parameterization also represents dry convection in the subcloud layer and nonprecipitating moist convection with a unified model. A detailed description of the EDMF scheme and its implementation is provided in Appendix A.

2.3. Convection Scheme

2.3.1. Tiedtke

The original Tiedtke mass-flux scheme (Tiedtke, 1989) has been modified by Zhang et al. (2011) for usage in WRF. It models shallow and deep convection separately, each using a plume that represents an ensemble

Table 1
Name of Simulations

Case	BL	Cu
MYNN_Tiedtke	MYNN	Tiedtke
EDMF_Tiedtke	EDMF	Tiedtke
MYNN_GFS	MYNN	GFS
EDMF_GFS	EDMF	GFS
MYNN_noCu	MYNN	NONE
EDMF_noCu	EDMF	NONE

of convective elements. The plume is initiated by the convective available potential energy within the subcloud layer and interacts with its environment via entrainment and cloud-top detrainment.

2.3.2. GFS

This is another mass-flux based (a Simplified Arakawa Schubert approach; Pan & Wu, 1995) convection scheme (Han & Pan, 2011) that differs from the Tiedtke scheme in the way the initiation, that is, trigger, of the convection and the entrainment to the modeled plumes are formulated. This scheme is designed to favor deeper clouds at the expense of shallower and stratiform (via large-scale saturation) clouds.

2.4. Other Parameterizations

The other common parameterizations employed in the simulations performed in this study are: MYNN (Nakanishi & Niino, 2006) surface flux parameterization (such that the modeling of the surface turbulent fluxes is consistent with the BL schemes), Rapid Radiative Transfer Model (RRTM) (Mlawer et al., 1997) for long wave radiation, Dudhia scheme (Dudhia, 1989) for short wave radiation and Morrison 2-moment scheme (Morrison et al., 2009) for the large-scale microphysics. The experiments, with corresponding parameterization combinations, are summarized in Table 1.

3. Mean Climate

Because of the zonally symmetric aquaplanet configuration and the prescribed hemispherically symmetric insolation, statistics shown below are averaged for 1 year after spin-up (the climate reaches equilibrium within 6 months), and then also averaged in longitude and over the two hemispheres.

3.1. Circulation

Primary features of the mean-state climate are large-scale circulations, such as the mean meridional overturning and the zonal winds. These are shown in Figure 1. Several common key features are observed. The mean meridional overturning, as represented by the mass-flux stream function, shows clockwise (positive) circulation spanning from the equator to approximately 30°N that is indicative of the Hadley circulation. It also exhibits a weaker anticlockwise circulation in the extratropics that represents the Ferell cell. Finally, a weak clockwise polar cell is seen poleward of 60°N. The zonally averaged zonal wind structure is similar for all the simulations with a strong upper-tropospheric jet at mid-latitudes of similar structure and strength. These features are in good qualitative agreement with other GCM simulations (e.g., Khouider et al., 2013; Williamson et al., 2012) as well as observations from reanalysis (e.g., Bengtsson et al., 2004; Pauluis et al., 2010, among many others).

Despite patterns that are similar across simulations, there are key quantitative differences in the strength of the generated Hadley cells, whose strength (computed as the maximum mass-flux stream function) ranges from $\sim 6.13\times10^{10}$ to $\sim 9.3\times10^{10}$ kg/s for the different simulations. The simulations with GFS, the most active convection scheme, generate the weakest Hadley cell strengths, whereas the simulations without a convection scheme generate the strongest (especially MYNN_noCu). Hadley cell strengths for simulations with Tiedtke lie in between these two extremes ($\sim 8.3\times10^{10}$ kg/s). We explore reasons behind these systematic differences in circulation strength in simulations with and without EDMF in section 4.1. The strength of the extratropical zonal jets shows smaller relative variability among simulations with maximum values ranging from $\sim$45 to $\sim$48.5 m/s. This peak occurs at the height of $\sim$12 km between $\sim 43^\circ$ and $\sim 45^\circ$ latitudes.

3.2. Thermal Structure

The humidity and cloud distributions are tightly coupled to the atmospheric circulation (Figure 2). The relative humidity (RH, calculated as the ratio of the water vapor mixing ratio to the saturation water vapor mixing ratio) distribution shows familiar features such as near saturation in the boundary layer irrespective of latitude, and strong horizontal and vertical variability in the free troposphere. In the tropics, moist and dry regions are, respectively, associated with the ascending and descending branches of the Hadley cell (Broginez & Pierrehumbert, 2007). Given that RH depends on both the atmospheric water vapor content and temperature, it is strongly influenced by dynamical processes, such as advection and convection (Pierrehumbert, 1998) as well as cloud microphysics (Pierrehumbert, 2002; Pierrehumbert et al., 2007). Thus,

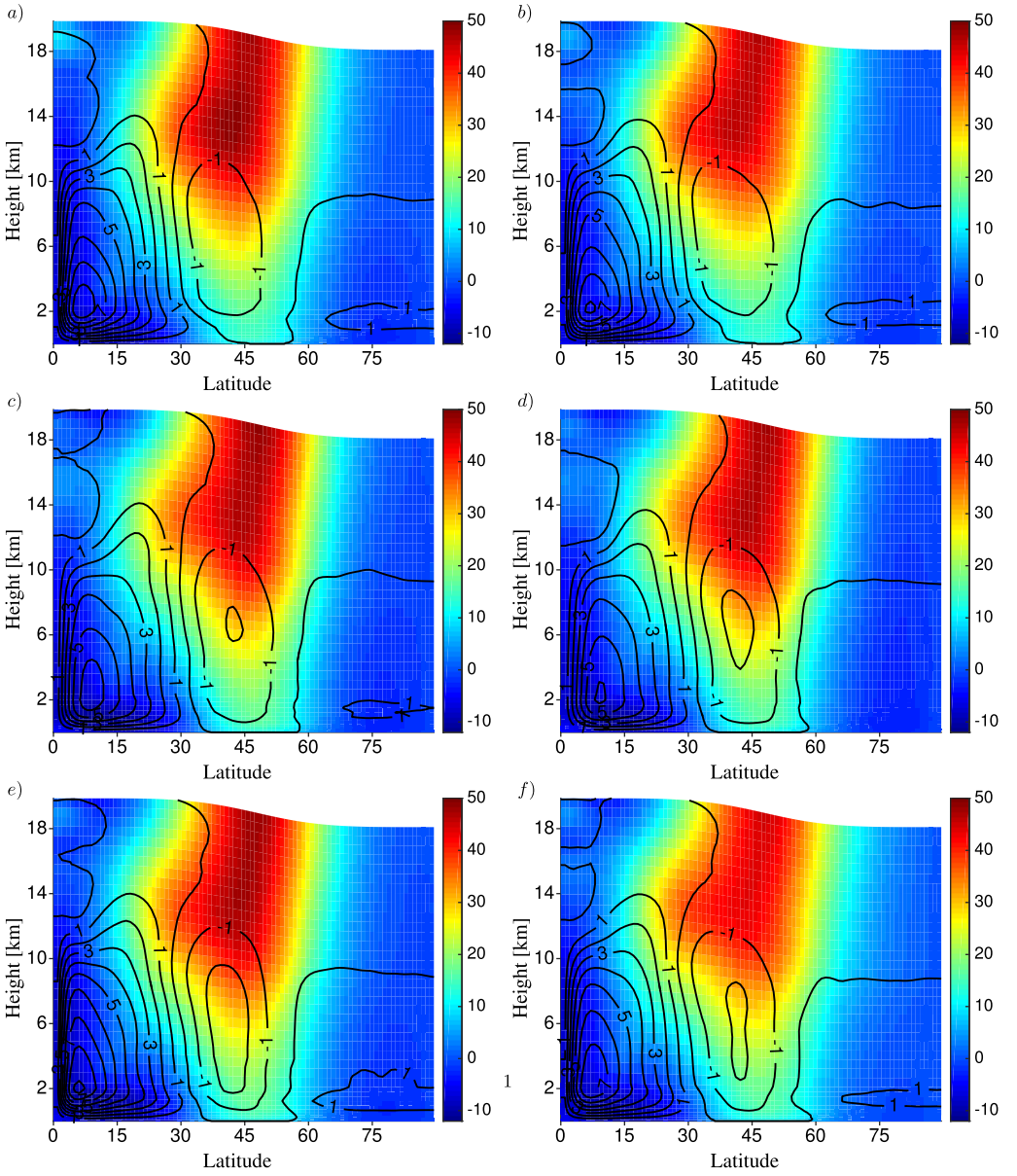

Figure 1. Zonal velocity (m/s) (color) and meridional mass-flux stream function (10^{10} kg/s) (line contours) for (a) MYNN_Tiedtke, (b) EDMF_Tiedtke, (c) MYNN_GFS, (d) EDMF_GFS, (e) MYNN_noCu, and (f) EDMF_noCu.

this distribution is somewhat sensitive to the convection scheme employed, a feature we will explore more in depth in section 4.2.

The cloud fraction structure shows deep clouds in the tropics, the presence of an outflow region in the tropical upper troposphere and shallow cloudiness throughout the globe. The ratio of shallow to deep clouds depends on the combination of the BL and the convection scheme employed. While the mean deep cloud fraction does not vary significantly across different simulations, we see a much bigger change in the average shallow clouds, from low for very active convection (GFS scheme, Figures 2c and 2d) to high for no convection scheme and a diffusivity type BL scheme (i.e., MYNN_noCu, Figure 2e). As discussed in section 4, these cloud changes have a strong impact on the atmospheric energy budget, and with it, on the global mean precipitation.

The zonal temperature and moist static energy (MSE) structure are shown in Figure 3. The MSE is the sum of three terms representing, respectively, the dry enthalpy, the latent energy, and the geopotential contributions:

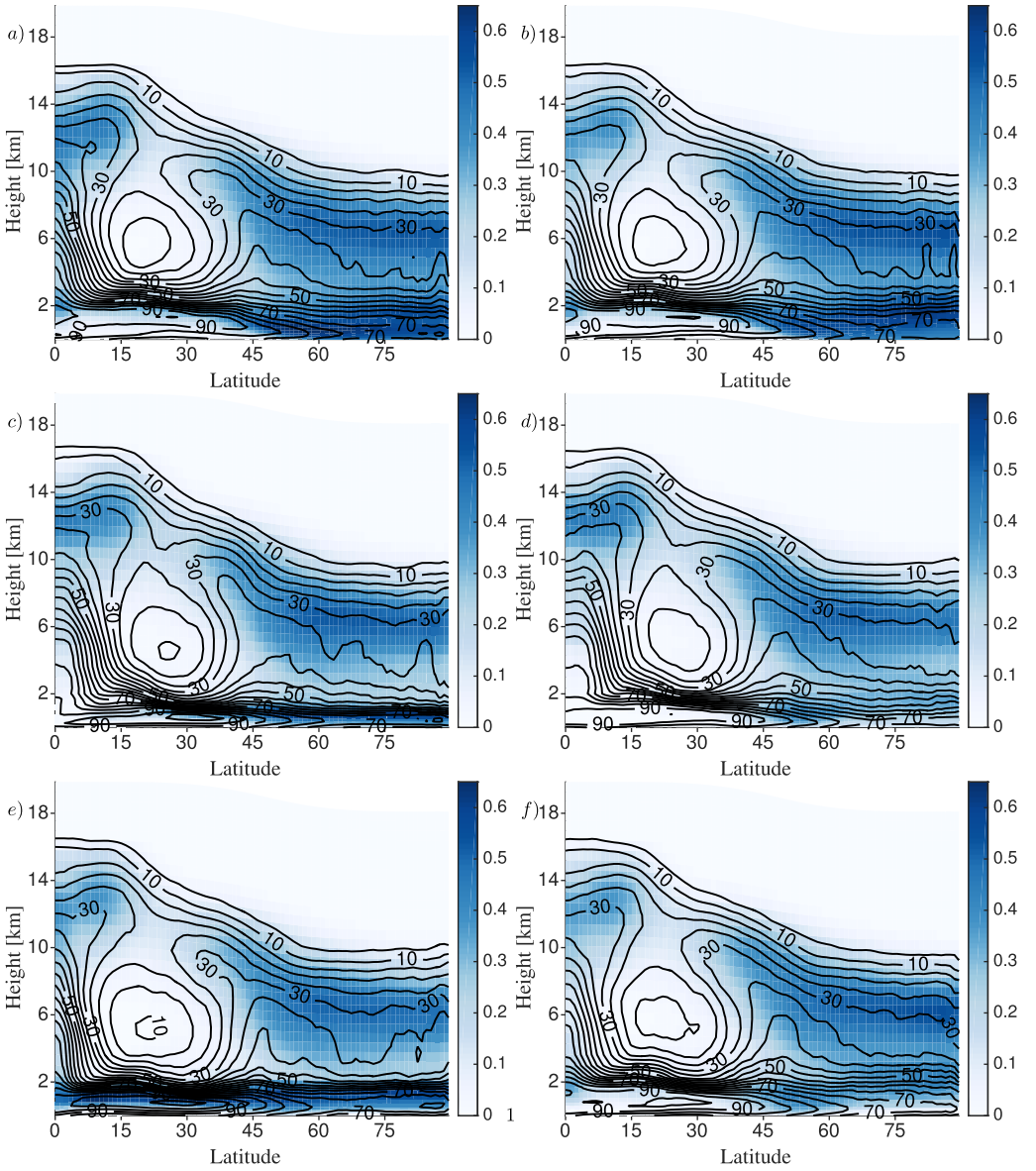

Figure 2. Cloud fraction (color) and relative humidity (line contours) for: (a) MYNN_Tiedtke, (b) EDMF_Tiedtke, (c) MYNN_GFS, (d) EDMF_GFS, (e) MYNN_noCu, and (f) EDMF_noCu.

$$MSE = C_p T + L_v q_v + gz, \tag{1}$$

where g is the gravitational acceleration, L_v is the latent heat of vaporization, C_p is the specific heat at constant pressure for dry air, T is the absolute temperature, z is the height above surface, and q_v is the water vapor mixing ratio. Expectedly, in the lower troposphere, both the temperature and the MSE peak at the equator for all the simulations. The temperature drops from approximately the prescribed SST near the surface to ~200 K high up in the troposphere. The lapse rate is approximately 6.5 K/km in the lower to middle troposphere. There are, however, quantitative differences in how the MSE is distributed horizontally and vertically for the different simulations. These differences are caused by how the differences in surface wind strengths generate different surface MSEs and by how the convection and the boundary layer schemes distribute the surface MSEs vertically. The distribution impacts (and is impacted upon by) the large-scale circulation. We discuss these differences more systematically in section 4.1.

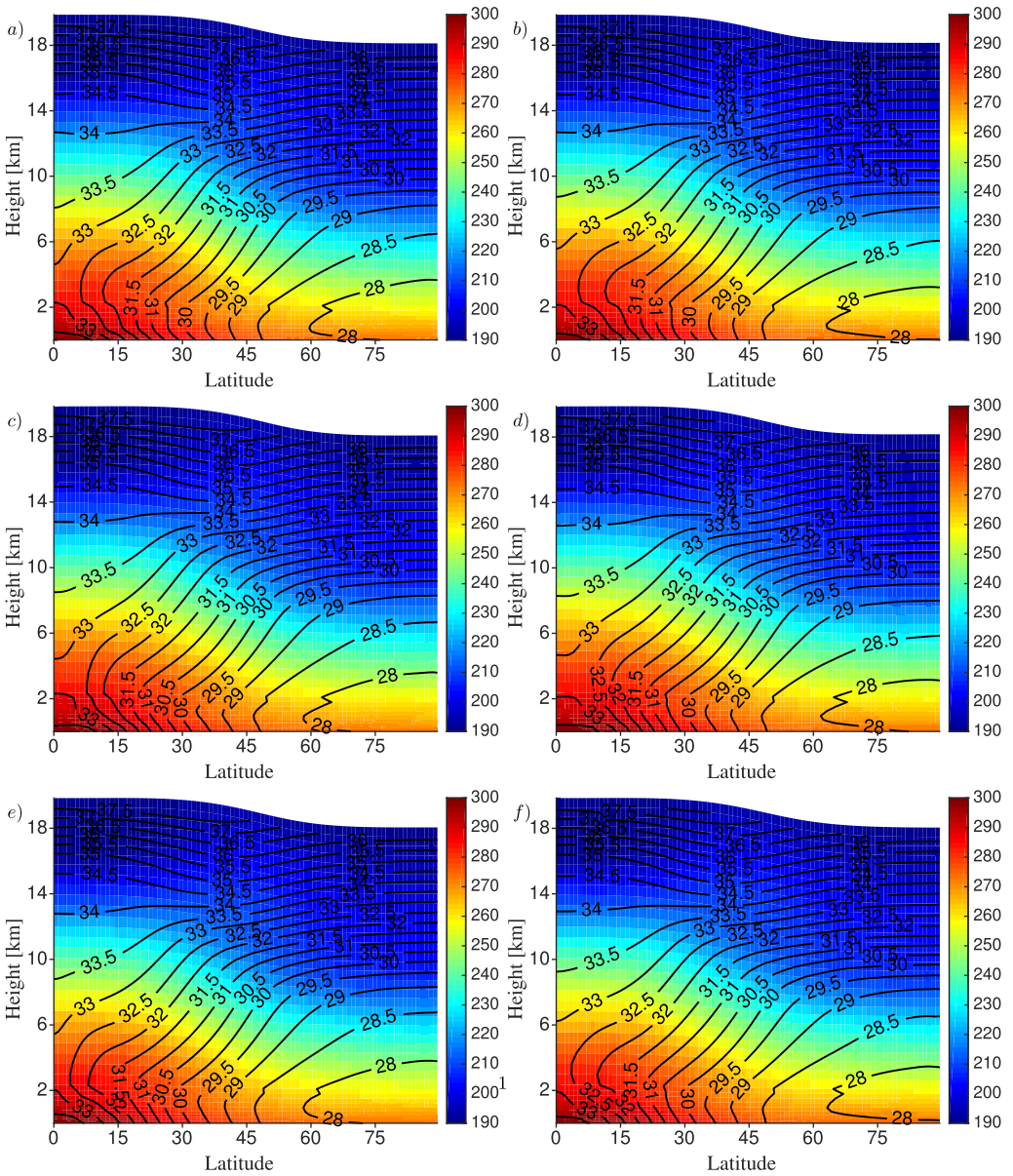

Figure 3. Zonal temperature (m/s) (color) and moist static energy line contours (10^5 J/kg) for: (a) MYNN_Tiedtke, (b) EDMF_Tiedtke, (c) MYNN_GFS, (d) EDMF_GFS, (e) MYNN_noCu, and (f) EDMF_noCu.

3.3. Surface Energy Budget

The generated cloud fraction profile has a clear imprint on the surface energy budget (Figure 4). The contributions to the budget are: net longwave at the surface (i.e., difference between the downward longwave radiation coming to and emitted from the surface), net shortwave at the surface (incoming minus reflected shortwave radiation), sensible heat flux, and latent heat flux. Positive values indicate downward fluxes. Specified SSTs for these simulations imply that the net energy fluxes at the surface are not necessarily in balance. Even so, for most of these simulations there is an approximate balance of energy at the surface with excess energy near the equator and the extratropics compensated by a deficit of energy in the subsidence regions in the subtropics as well as in the polar regions: a result of the SSTs being prescribed from a case in equilibrium (Williamson et al., 2012).

Several commonalities are seen in the zonal structure of the fluxes. The net shortwave radiation has an off-equatorial maximum for all the simulations due to extensive cloudiness especially at the ITCZ at the equator (note the specified insolation at the top of the atmosphere is maximum at the equator throughout the

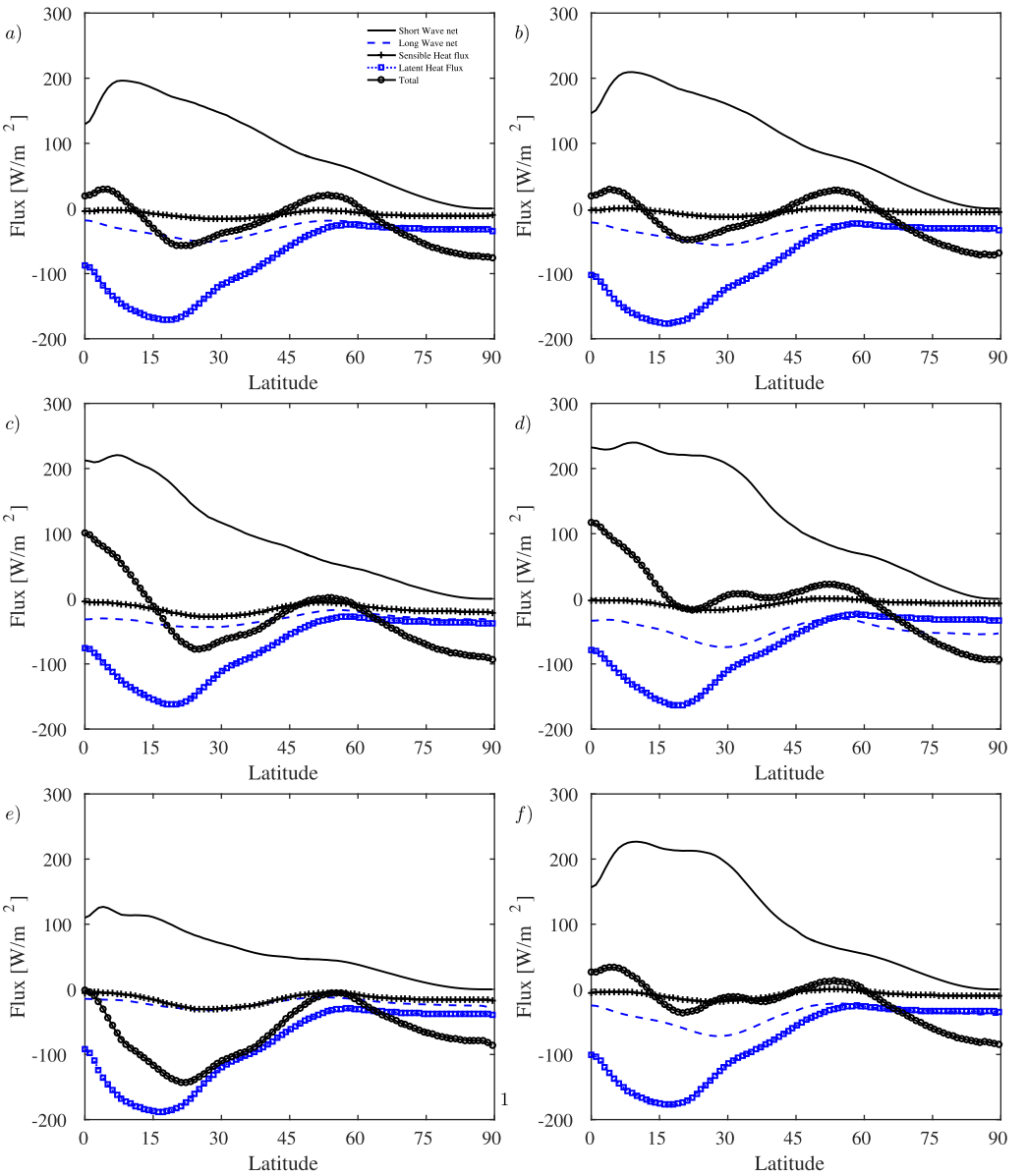

Figure 4. Surface energy budget for: (a) MYNN_Tiedtke, (b) EDMF_Tiedtke, (c) MYNN_GFS, (d) EDMF_GFS, (e) MYNN_noCu, and (f) EDMF_noCu.

simulations). The net longwave radiation does not contribute substantially to the energy budget because of the presence of large ratios of water vapor and clouds in the lower troposphere. The surface nonradiative fluxes are dominated by the latent heat flux that shows similar zonal structure and magnitude in all simulations: a maximum in the subsidence regions within the tropics, a structural feature noted in other aquaplanet simulations (Medeiros et al., 2016; Williamson et al., 2012). The simulation MYNN_noCu behaves the most differently from the other simulations owing to the lack of a convection scheme and a purely diffusive BL scheme. This implies enhanced cloudiness near the surface throughout the globe resulting in a much reduced incoming shortwave at the surface.

4. Sensitivity to the Parameterizations

4.1. Precipitation Structure

While the generated climate states are qualitatively similar, there are some crucial differences among the simulations. In addition to the ones highlighted above, a major difference can be noted in the generated

Table 2
Net Global Mean Precipitation and Radiative Cooling

Case	Precipitation (mm/d)	Radiative cooling (K/d)
MYNN_Tiedtke	3.675	1.039
EDMF_Tiedtke	3.722	1.045
MYNN_GFS	3.105	1.031
EDMF_GFS	3.028	0.96
MYNN_noCu	3.885	1.158
EDMF_noCu	3.484	1.036

precipitation and its partitioning between convective and grid-scale precipitation. Table 2 lists the values of global mean precipitation across simulations, while Figure 5 shows the latitude distribution of mean precipitation and the convective precipitation to grid-scale precipitation ratio for EDMF and MYNN for each of the three convection schemes. The zonal structure of precipitation is similar across the six simulations, with a tropical absolute maximum near the equator (associated with the Intertropical Convergence Zone) and another weaker local maximum in the extratropics in association with storm tracks at those latitudes. This structure broadly resembles what is observed in other aquaplanet simulations (Medeiros et al., 2008; Williamson et al., 2012).

However, a remarkable sensitivity of the net precipitation amount to the employed convection scheme is noted. With Tiedtke, the maximum mean precipitation rate (near the equator) is approximately 25 mm/d (Figure 5a). With the more active GFS convection scheme (Han & Pan, 2011), this rate reduces to around 12 mm/d (Figure 5b). When no convection scheme is employed (with a diffusive BL scheme), the maximum precipitation rate increases to ∼35 mm/d (Figure 5c). The global mean precipitation amount is driven by the balance between radiative cooling in the troposphere and the condensational latent heating (a major fraction of the condensate is the surface precipitation) (O'Gorman et al., 2012). This balance is clearly evident in the global tendencies generated by the different parameterizations (we discuss these tendencies and explore them for the deep tropics in section 4.2).

Here we focus on the global radiative cooling tendencies for the six simulations (with global mean values listed in Table 2, and vertical profiles for all simulations shown in Figure 6). Radiative cooling can occur via longwave emission (whose difference among simulations is primarily controlled by differences in generated deep clouds) or via shortwave reflection (linked to shallow clouds). As mentioned in section 3.2, while the

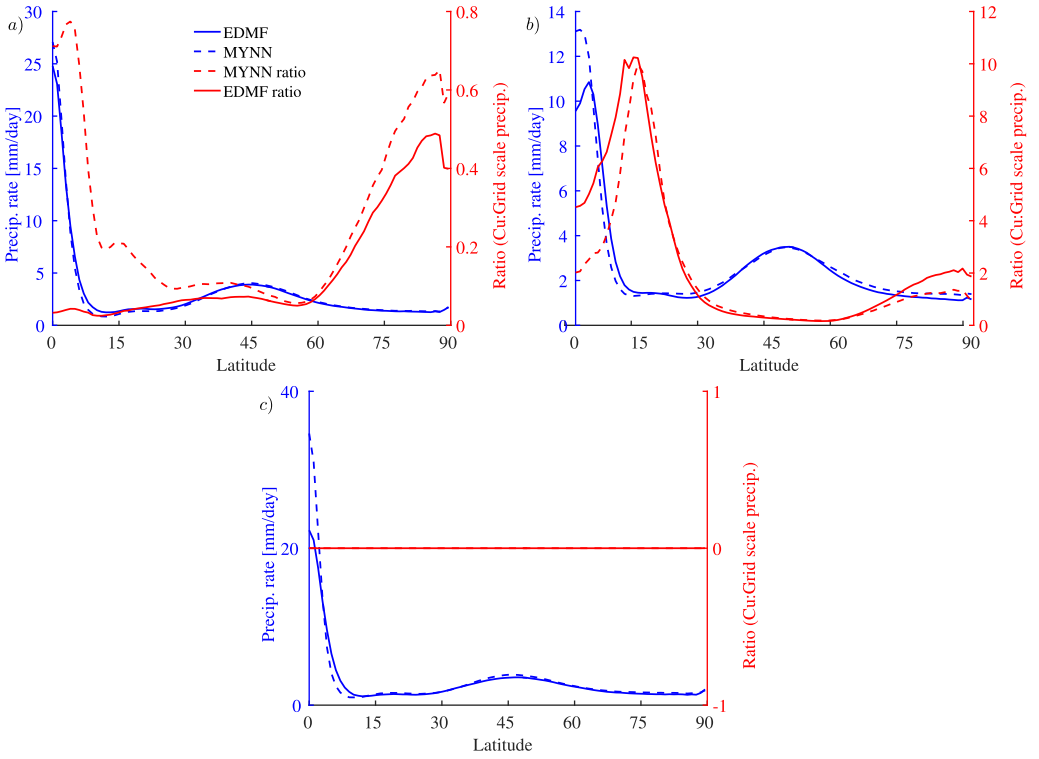

Figure 5. Mean precipitation (blue, left axis) and ratio of its convective to grid-scale contributions (red, right axis) for (a) MYNN_Tiedtke and EDMF_Tiedtke, (b) MYNN_GFS and EDMF_GFS, and (c) MYNN_noCu and EDMF_noCu. Global mean precipitation values are presented in Table 2.

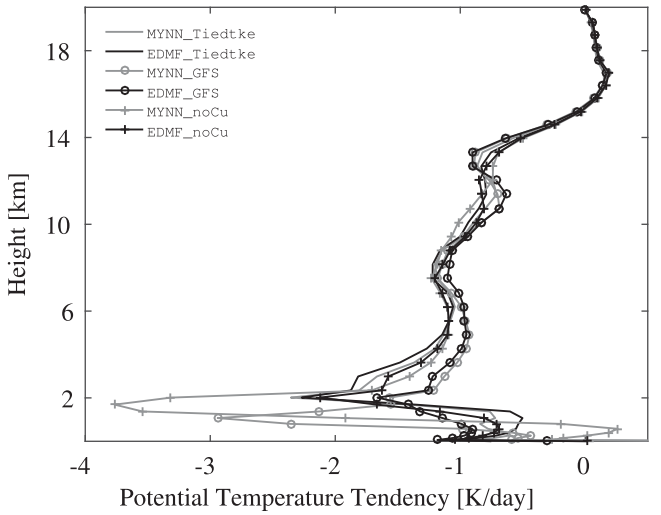

Figure 6. Global radiative cooling profiles (shortwave + longwave) for the six simulations. Global mean radiative cooling values are presented in Table 2.

mean deep cloud fraction does not vary substantially among simulations, the shallow cloud fraction shows significant changes. This is evident in Figure 6, which shows that the spread in low-level cooling is much larger than that in high-level cooling. With mostly shallow clouds (no convection scheme, diffusive BL: MYNN_noCu), stronger net radiative cooling (∼1.16 K/d) implies enhanced mean precipitation (global mean ∼3.9 mm/d). On the opposite end, a very active convection scheme (GFS) favoring deep clouds (Han & Pan, 2011) leads to less net radiative cooling (∼1 K/d) resulting in reduced mean precipitation (global mean ∼3.1 mm/d). When Tiedtke (radiative cooling ∼1.04 K/d) is used, the generated global mean precipitation lies in between these two limits (∼3.7 mm/d). Without a convection scheme (Figure 5c), the precipitation amount also depends crucially on the BL scheme. Thus, adding a mass-flux component to the BL scheme (that is, changing from MYNN_noCu to EDMF_noCu) leads to reduced saturation near the surface with a corresponding reduction in the net radiative cooling (from ∼1.16 K/d to ∼1.04 mm/d) and hence to a reduction in the mean precipitation from ∼3.9 to ∼3.5 mm/d.

Even though the net precipitation is similar for a given convection scheme, its partitioning into convective and grid-scale precipitation depends crucially on the BL scheme, especially in the ITCZ where convection is the most active. The reason for this sensitivity lies in the interaction between the BL and the convection scheme. The BL scheme determines the properties of the subcloud layer which, along with the large-scale flow features, dictates the frequency and location of activation of the convection scheme as well as the amount of vertical instability (difference of MSE between the subcloud and the cloudy layer) that the convection scheme dissipates (Moebis & Stevens, 2012; Numaguti, 1993; Prive & Plumb, 2007). The interaction between deep convection and the large-scale circulation, directly and via the BL scheme, is a complex problem that has been extensively studied over a range of scales. One side of this interaction involves how the large-scale circulation preconditions deep convection. For example, over scales of the size of tropical storms, weaker deep convection leads to weaker ascending motions that eventually lead to weaker moisture convergence at the base of the storm causing a positive feedback (Trenberth et al., 2003). Over larger scales, the MSE within the BL is a crucial element in the activation of moist convection (Emmanuel et al., 1994; Neelin & Held, 1987; Prive & Plumb, 2007). Near-surface winds (which are determined by the strength of the circulation) determine the distribution of near-surface MSE (Moebis & Stevens, 2012). This MSE is then vertically distributed within the subcloud layer and shallow cloudy layers differently by different BL schemes (as we see in section 4.2). The MSE content of the BL and its vertical profile determine the location and strength of activation of moist convection (Moebis & Stevens, 2012; Numaguti, 1993).

Convection, in turn, transports heat and moisture vertically leading to vertical homogenization of MSE in regions of ascending motions within the tropics (Spencer et al., 2015). The vertical distribution of MSE determines the gross moist stability, that is, the effective energy stratification felt by the Hadley cell (Held, 2000; Neelin & Held, 1987; Spencer et al., 2015), one of the key factors controlling the Hadley cell strength and its response to radiative perturbations (Feldl & Bordoni, 2016). Additionally, the Hadley cell strength has been shown to be sensitive to the zonally averaged MSE gradient between the extratropics and the tropics (Held, 2000; Held & Hou, 1980), and hence to any factor, such as the strength of convection, that might influence this gradient (Seo et al., 2014). The influence of convection on tropical clouds and, associated radiative effects, can also influence the circulation strength and structure as well as their sensitivity to perturbations (Voigt & Shaw, 2015). Finally, vertical momentum mixing associated with convection can affect the circulation strength primarily through changes in the Coriolis torque (Han & Pan, 2011; Richter & Rasch, 2008). These interactions and feedbacks make the interaction of convection (and how it is parameterized in numerical models) and the large-scale dynamics a very involved problem (Mapes, 1997; Raymond et al., 2009).

Here we show how the choice of the BL scheme influences the simulated circulation (measured as the mass-flux stream function) and the associated MSE distribution (Figure 7). We focus on the tropospheric MSE distributions in the tropics and the subtropics and their link to the Hadley circulation. We discuss the

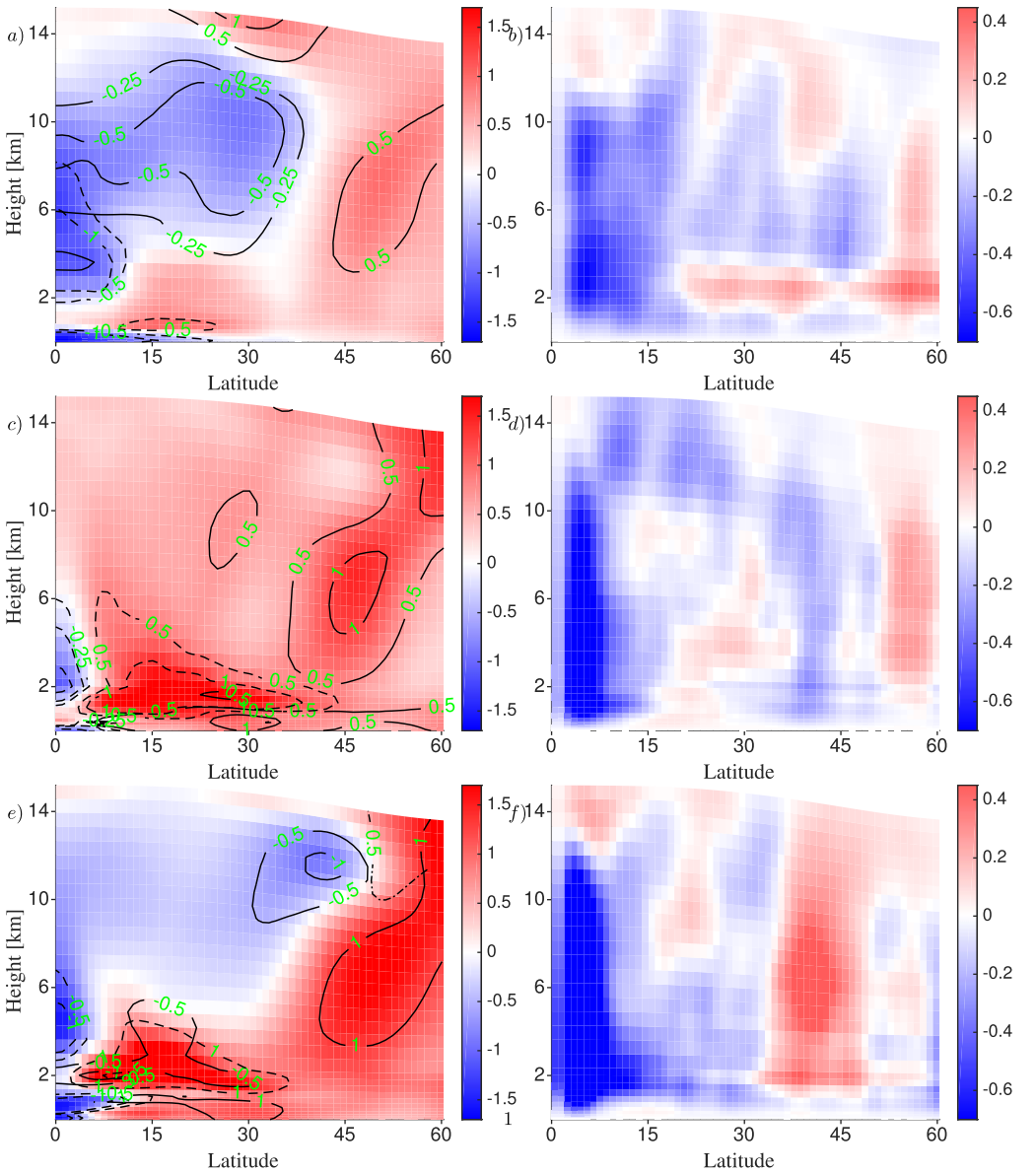

Figure 7. MSE (left, in 10^3 J/kg) and circulation (right, in 10^{10} kg/s) differences between (a, b) EDMF_Tiedtke and MYNN_Tiedtke, (c, d) EDMF_GFS and MYNN_GFS, and (e, f) EDMF_noCu and MYNN_noCu. The line contours represent the differences in temperature (solid line) and moisture (dashed lines) contributions, respectively, to the MSE differences.

MSE differences between simulations with and without EDMF and how these differences arise from contributions from dry enthalpy (i.e., temperature) and latent energy (i.e., moisture). Differences in geopotential are small within the troposphere and are omitted in Figure 7 for the sake of clarity. For each of the three convection schemes, within the ITCZ, EDMF is associated with a deeper vertical extent of moisture distribution (including shallow cloud layer in addition to the subcloud layer) than MYNN (as seen in the moisture tendency profiles discussed in section 4.2, Figure 9). EDMF is also associated with larger heating in the subcloud layer and cooling aloft in the shallow cloud layers (also see Figure 8 from section 4.2), but the enhanced moisture transport more than compensates for that in terms of the MSE distribution. As a consequence, there is a reduction of MSE near the surface and increase in shallow cloud-layer MSE, common for all the EDMF simulations. This change in vertical MSE distribution near the surface at the ITCZ activates the convection differently, the net impact of which, on the distribution of moisture, temperature and, hence, MSE also depends on the large-scale circulation and the microphysics scheme. For all cases, there is a net reduction of water vapor (and MSE) from ~2 to ~6 km height at the ITCZ and variable degrees of drying and

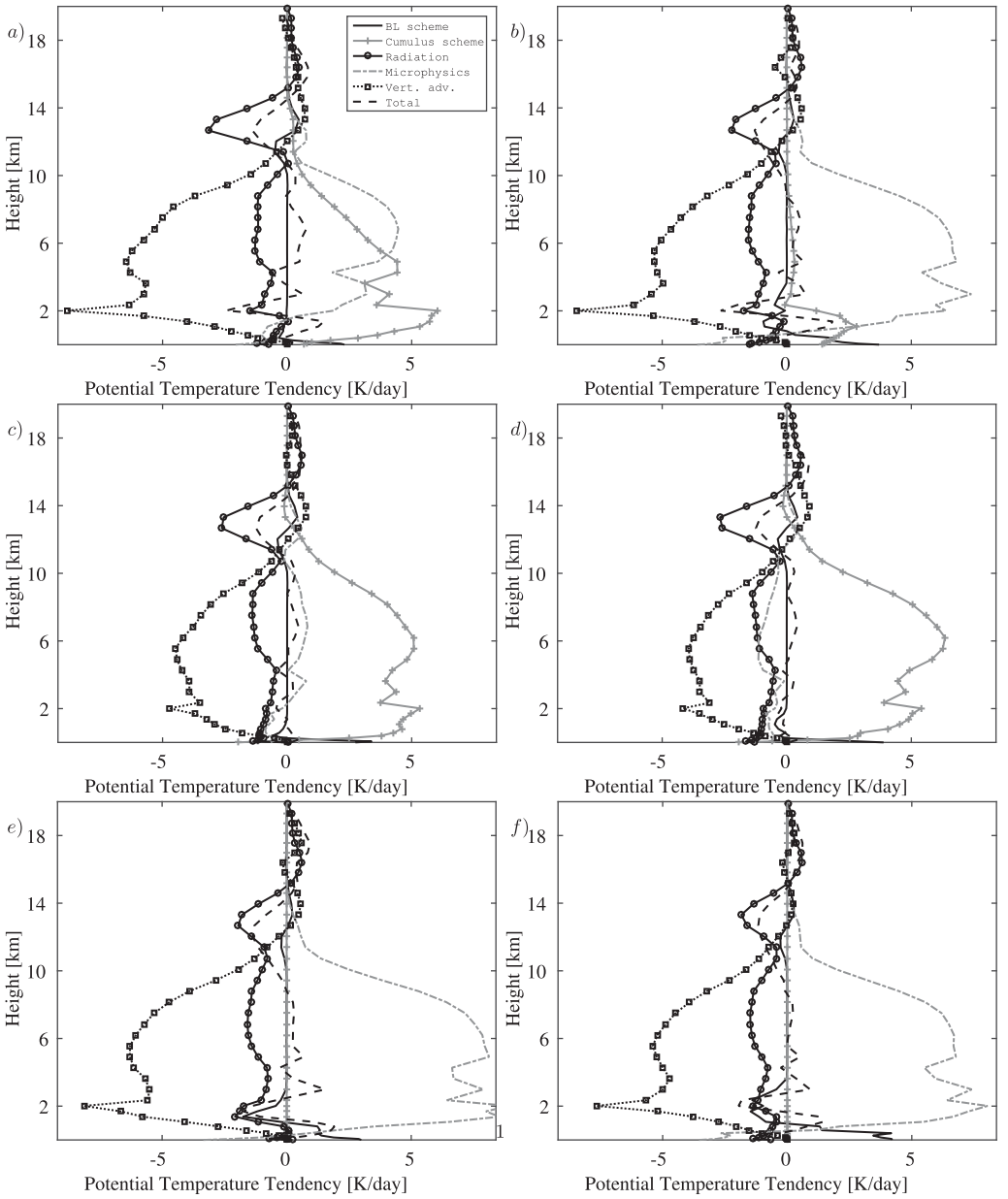

Figure 8. Vertical profiles of potential temperature tendencies from different parameterizations in the deep tropics (5°S–5°N) for: (a) MYNN_Tiedtke, (b) EDMF_Tiedtke, (c) MYNN_GFS, (d) EDMF_GFS, (e) MYNN_noCu, and (f) EDMF_noCu.

cooling above that. Beyond the ITCZ, in the subtropics, there is an increase of MSE in the shallow layers in simulations with EDMF. This is associated with reduced drying in the descending branch of the weakened Hadley circulation. In accordance with the discussion above, these differences in the horizontal and the vertical MSE distributions imprint on the Hadley cell differences, with EDMF generating a weaker Hadley cell overall (the maximum differences in mass-flux stream function are $\sim$2.14, $\sim$ .69, and $\sim$1.17 (in 10^{10} kg/s) for no convection, Tiedtke, and GFS respectively). The corresponding differences in peak Hadley cell strengths are $\sim$1.3, $\sim$ 0.54, and $\sim$0.33 (in 10^{10} kg/s) respectively. Note that we select the absolute stream function maximum, rather than the maximum value at a specified latitude and height, as a measure of the Hadley cell strength.

4.2. Tendencies of Potential Temperature and Moisture

To investigate how the various subgrid parameterizations interact with the large-scale flow and how this interaction depends on the choice of the convection-boundary layer scheme combination, we consider the

tendencies of potential temperature and water vapor in equilibrium. Tendencies such as these have been used to evaluate GCMs (Del Genio et al., 1991; Knutson & Manabe, 1995) as well as to estimate biases in weather models when compared to observations (Cavallo et al., 2016; Williams & Brooks, 2008). The thermodynamic equation being solved for in WRF is (Skamarock et al., 2008):

$$\bar{\theta}_t + m^2[\partial_x(\bar{u}\bar{\theta}) + \partial_y(\bar{v}\bar{\theta})] + m\partial_\eta(\bar{\omega}\bar{\theta}) = F\bar{\theta}, \tag{2}$$

wherein t, x, y, and η are time, horizontal, and vertical coordinates, respectively. The subscript indicates the corresponding partial derivative. $\bar{\theta}$, $\bar{u}$, $\bar{v}$, and $\bar{\omega}$ represent the grid-mean potential temperature, zonal and meridional winds, and pressure velocity multiplied by the mass of dry air within a grid box. m is the map projection factor used to map the WRF projections (Lambert conformal, polar strereographic, and Mercator) onto the Earth's surface. F_Θ on the rhs represents the combination of the forcing terms. An analogous equation for water vapor mixing ratio is also solved in WRF wherein $F_{\bar{q}_v}$ represents the forcing term of the mixing ratio. The forcing term $F_{\bar{\theta}}$ is decomposed as:

$$F_{\bar{\theta}} = F_{\bar{\theta},radiation} + F_{\bar{\theta},cumulus} + F_{\bar{\theta},pbl} + F_{\bar{\theta},mixing/diffusion} + F_{\bar{\theta},microphysics}. \tag{3}$$

The first four terms in the rhs, respectively, represent the tendencies due to radiation, cumulus, boundary layer (pbl) schemes, and subgrid horizontal mixing (which is set to zero). A Runge-Kutta three step integration is performed in time at the end of which an adjustment due to the cloud microphysics is carried out explicitly. We explore the tendencies due to the radiation, the cumulus, the BL, and the microphysics schemes. We also compute the cooling by the large-scale vertical transport. The sum of all these tendencies needs to balance the resolved horizontal mixing/transport (which are not computed explicitly in WRF) in equilibrium. The global sum of the parameterized and the resolved vertical tendencies is found to be very close to zero confirming equilibrium. We focus on the deep tropics (5°S–5°N), where convection is the most active and, hence, where the tendencies are the most sensitive to the convection-boundary layer scheme combination. The potential temperature and the water vapor mixing ratio tendencies in this region are shown in Figures 8 and 9, respectively.

Above the subcloud layer, the two cumulative tendencies, respectively, show a dominant balance between atmospheric cooling and moistening by large-scale lifting and heating and drying by both the cumulus and the microphysics scheme. Within the subcloud layer, the microphysics scheme evaporatively cools and moistens. The magnitude of the radiative cooling tendency is dominant only near the top of the atmosphere (it has a value of $\sim$2 K/d throughout the troposphere; a feature that is reasonably consistent across simulations), while that of the boundary layer scheme tendency is, not surprisingly, only significant near the surface.

The nature of the balance of tendencies does depend significantly on the convection-boundary layer scheme combination. The primary dependence is on the convection scheme that governs the dominant cloud regime (Williams & Brooks, 2008), while the BL scheme acts to modify this dependence by influencing the activation of the convection scheme (location and frequency) as mentioned in section 4.1. In terms of the tendency magnitudes (when compared to Tiedtke or no convection scheme), the GFS scheme (MYNN_GFS and EDMF_GFS: Figures 8c and 8d and Figures 9c and 9d) leads to a substantially weaker lifting of moisture, which is also evident in the much lower rain rate in the deep tropics (Figure 5b). The weakening of the circulation (as was also noted in section 3.1) results from a combination of factors including the magnitude and shape of the heating profile as well as the modified (in-cloud pressure gradients being included in the formulation in addition to lateral entrainment and detrainment rates, as in Tiedtke) momentum mixing induced by this scheme (Han & Pan, 2011). Since it favors convective rain and deep convection, the lifting of moisture is predominantly balanced by the convective condensation with GFS.

Next we consider how the BL scheme impacts the convective tendencies. Simulations with EDMF have temperature tendencies from the boundary layer scheme that are stronger than those with MYNN. The mass-flux component that advectively transports heat and moisture upward is responsible for this difference. EDMF tends to cause stronger heating near the surface and cooling of the shallower cloudy layers, while MYNN mixes heat within just the subcloud layer. Concurrently, EDMF transports surface water vapor to greater depth when compared to MYNN (Figure 7). These differences influence the activation of the convection scheme. For example, Tiedtke activates more sparingly in response to this homogenization by EDMF

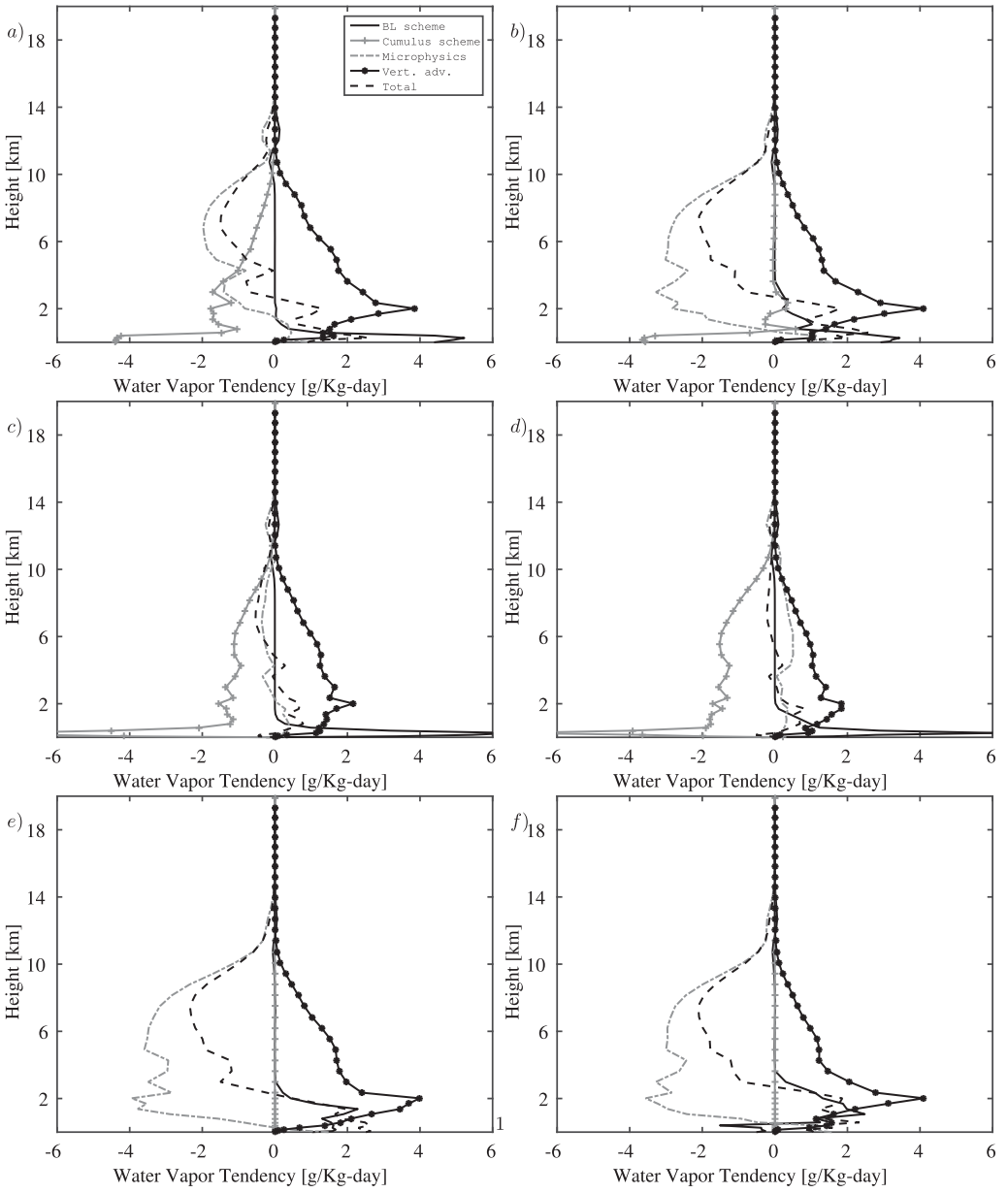

Figure 9. Vertical profiles of water vapor mixing ratio tendencies from different parameterizations in the deep tropics (5°S–5°N) for: (a) MYNN_Tiedtke, (b) EDMF_Tiedtke, (c) MYNN_GFS, (d) EDMF_GFS, (e) MYNN_noCu, and (f) EDMF_noCu.

(Figures 8a and 8b and Figures 9a and 9b). The signature of this reduction in activation of Tiedtke is also seen in Figure 5a where the convective to grid-scale precipitation ratio drops drastically at the ITCZ near the equator with the usage of EDMF. With GFS, we see similar smaller BL tendencies at lower levels. However, since GFS generates deeper clouds at the expense of shallower clouds (Han & Pan, 2011) the microphysics scheme causes more evaporation (of falling rain) than condensation with EDMF (overall negative tendency). We can notice this in Figure 7c, where, with GFS, EDMF is not associated with an overall reduction in water vapor in the entire vertical column in the deep tropics. This causes the cumulus terms to increase somewhat in the deeper layers. In the absence of a convection scheme, the balance of tendencies is qualitatively insensitive to the BL scheme: only the circulation strength, and, correspondingly, the microphysics tendency reduces with EDMF, Figure 7e. The diversity in these features highlights how the BL scheme and the convection scheme interact with each other in nontrivial ways and through many different

pathways, involving subcloud dynamics, large-scale flow and microphysics. The balance of these tendencies (and how they evolve with climate change) form an important component in the development of climate models and their employed parameterizations (Chikhar & Gauthier, 2015; Collins et al., 2006; Park & Bretherton, 2009)

5. Conclusions and Discussions

How do various subgrid parameterizations interact to generate mean climate states in global models? We perform aquaplanet simulations using the global Weather Research and Forecast (WRF) model and a wide range of parameterizations to start addressing this question in a simplified setting. The parameterizations we focus on are the convection and the BL schemes, which are primarily responsible for dissipating vertical instabilities. Six simulations are performed: with a very active, deep-heating convection scheme (GFS), a moderately active convection scheme (Tiedtke), and no convection scheme, each with MYNN or EDMF as the employed BL scheme. EDMF adds a mass-flux component to the purely diffusive MYNN scheme. This component models updrafts within the BL that stochastically interact with their environment and advectively transport moisture and heat vertically. This results in a more realistic coupling between the subcloud layer and the cloudy layers above.

The generated mean climates behave reasonably in terms of qualitative mean dynamic, thermodynamic, and radiative features. The peak strength of the Hadley circulation varies inversely with the strength of the employed convection scheme. While the precipitation distribution with latitude is fairly reasonable and similar to that of other aquaplanet simulations, its amount depends strongly on the convection scheme. The dependence is particularly strong at the ITCZ, where the precipitation is mainly generated by the deep clouds. Here an inverse relationship between the strength of the convection scheme and the total precipitation exists, a feature explained by the global energy budget being primarily maintained by a balance between atmospheric cooling and condensational heating. In addition, the partitioning of precipitation into convective and grid-scale components is also dependent on the employed BL scheme that preconditions the activation of the convection scheme.

To explore how the parameterizations interact with each other to generate different simulated climates, we investigate the potential temperature and moisture tendencies focusing primarily on the deep tropics, where the biggest differences exist. The dominant balance above the subcloud layer is between the cooling and moistening by resolved lifting and heating and drying due to condensation (modeled in part by both the convection and the microphysics schemes). Radiative cooling is dominant at the top of the troposphere, whereas the BL scheme is a significant factor within the subcloud layer. The strongest convection scheme (GFS) leads to an on-average weaker vertical advection of moisture that results in weaker precipitation. The most abundant precipitation is found in the simulation with no convection scheme, and a diffusive boundary layer scheme, which produces strong radiative cooling of the atmosphere by a dense layer of shallow clouds that needs to be balanced by condensational heating.

The BL scheme distributes MSE near the surface (by vertical mixing and via its impact on the near-surface winds (Zhang & Zheng, 2004)) and hence plays a role in the activation of the convection scheme. The EDMF transports moisture deeper into the shallow cloudy layer atop the subcloud layer when compared to the MYNN. It also heats the subcloud layer resulting in cooling of the shallow cloudy layer, while the MYNN diffusively mixes heat just within the subcloud layer. These different MSE distributions lead to differential activations of the convection scheme in terms of both location and frequency. The mean climate is maintained by very different balances of tendencies depending on the strength of the convection scheme and its rate of activation.

A detailed analysis of the profiles of the different tendencies (from the different physical processes) for both potential temperature and water vapor is performed. A key conclusion from the study of these tendencies is that similar climates with similar vertically distributed energy and water balances in the tropics can be obtained with significantly different profiles of large-scale, convection and microphysics tendencies generated from diverse combinations of model parameterizations. This might be reflective of the extensive tuning that is usually performed when new parameterizations are implemented in GCMs to reproduce the present-day climate. The differences in generated vertical heating profiles, despite similar mean-state climates, when different parameterizations are used in WRF do suggest the importance of

evaluating model simulations against observed heating profiles. These comparisons, together with the continued development of physically based parameterizations, might lead to improved representation of processes that are not explicitly resolved by current climate models to generate correct mean climatic states and their response to perturbations in a physically consistent manner.

Appendix A: Mass-Flux Parameterization Within EDMF

In this version of the model, the mass-flux parameterization models multiple steady-state laterally entraining (dry or moist, but nonprecipitating) updrafts. All updrafts are initiated at the surface. The steady-state updraft equation for the updraft mean variables $\bar{\varphi}_i=\{\bar{\theta}_{li}, \bar{q}_{ti}, \bar{u}_i, \bar{v}_i\}$ (liquid water potential temperature, total water mixing ratio, and two horizontal velocity components, respectively: note the thermodynamic variables being used are moist conserved) in the ith updraft can be written as:

$$\partial_z \bar{\varphi}_i = \varepsilon_i(\bar{\varphi}-\bar{\varphi}_i), \tag{A1}$$

where ε_i represents the entrainment rate for the ith updraft.

The updraft vertical velocity is solved for by using the difference between the buoyancy and the drag force on an air parcel:

$$\frac{1}{2}\partial_z \bar{w}_i^2 = a_w B_i - (b_w + c_w\varepsilon)\bar{w}_i^2, \tag{A2}$$

where $B_i=g(\bar{\theta}_{vi}/\bar{\theta}_v-1)$ is the buoyancy of the ith updraft. $a_w=2/3$, $b_w=0.002$, and $c_w=1.5$ are constants that parameterize pressure and subplume variability impacts on the plume vertical velocity (de Roode et al., 2012). This form of the vertical velocity equation has been used in Suselj et al. (2012, 2013).

Ten updrafts ($i=1\ldots I$, with $I=10$) are initialized at the surface, each with different surface conditions: they are integrated in the vertical and each of them experiences an entrainment rate that encapsulates its interaction with its environment. Integration for each updraft is done independently up to one model level below the level at which the vertical velocity becomes negative. Water vapor in the ith updraft is assumed to condense at the model level where the mean updraft total water exceeds the saturated mixing ratio (i.e., where $\bar{q}_{ti}(z) > \bar{q}_{si}(\bar{T}_i(z), p(z))$). Upon saturation, the liquid water is the water excess relative to the saturated mixing ratio, $\bar{q}_{li}=\bar{q}_{ti}-\bar{q}_{si}$. To close this set of equations, we need formulations for the surface boundary conditions and for the entrainment. These are described next.

A1. Surface Conditions for the Mass-Flux

Updraft boundary conditions at the surface are parameterized following Cheinet (2003). Gaussian probability density functions (PDF) of vertical velocity, total water mixing ratio, and virtual potential temperature are prescribed at the surface. PDF mean values are taken to be the grid-mean values of the corresponding variables, and the second moments (variance of the Gaussian PDF: for example, $\sigma_w{}^2$ for vertical velocity) are parameterized. The updrafts are assumed to represent the tail of this vertical velocity distribution. Total water mixing ratio and virtual potential temperature in the updrafts are then computed based on both their PDFs as well as their correlations with the vertical velocity. The process is described in more details below.

Cumulatively, all updrafts represent areas with near-surface vertical velocity exceeding w_{min}. For numerical purpose, we assume that the near-surface vertical velocity is limited by w_{max}. The cumulative fraction of the area of all I updrafts is thus:

$$\sum_{i=1}^{I} a_i = \frac{1}{2}\left[\mathrm{erf}\left(\frac{w_{\max}}{\sqrt{2}\sigma_w}\right) - \mathrm{erf}\left(\frac{w_{\min}}{\sqrt{2}\sigma_w}\right)\right]. \tag{A3}$$

We prescribe $w_{\max}=3\sigma_w$ and $w_{\min}=0.5\sigma_w$. These yield a surface updraft fractional area $\approx 30\%$. The surface updraft conditions for each of the I updrafts are obtained by linearly (in terms of the vertical velocity) discretizing the PDF between w_{min} and w_{max} so that the vertical velocity of the ith updraft is:

$$\bar{w}_i = w_{\min} + \Delta w\left(i + \frac{1}{2}\right), \tag{A4}$$

with $\Delta w \equiv (w_{\max} - w_{\min})/I$. The fractional area of the ith updraft is thus obtained by integrating the PDF of vertical velocity from $w_i - \frac{1}{2}\Delta w$ to $w_i + \frac{1}{2}\Delta w$:

$$a_i = \frac{1}{2}\left[\mathrm{erf}\left(\frac{w_i + \frac{1}{2}\Delta w}{\sqrt{2}\sigma_w}\right) - \mathrm{erf}\left(\frac{w_i - \frac{1}{2}\Delta w}{\sqrt{2}\sigma_w}\right)\right]. \tag{A5}$$

Having obtained the updraft vertical velocity, the updraft virtual potential temperature, and the updraft total water mixing ratio for the ith plume are obtained using:

$$\bar{\theta}_{v,i} = \bar{\theta}_v|_s + c(w, \theta_v)\bar{w}_i \frac{\sigma_{\theta_v}}{\sigma_w}, \tag{A6}$$

$$\bar{q}_{t,i} = \bar{q}_t|_s + c(w, q_t)\bar{w}_i \frac{\sigma_{q_t}}{\sigma_w}. \tag{A7}$$

Symbols $\bar{\theta}_v|_s$ and $\bar{q}_t|_s$ represent the mean surface (first model level) values of the corresponding variables. The correlation coefficients between the vertical velocity and virtual potential temperature ($c(w, \theta)$) and total water mixing ratio ($c(w, q_t)$) are taken to be 0.58. Note that we take $c(w, q_t)$ to be equal to $c(w, \theta_v)$ instead of having a value of 0.32 as in Cheinet (2003). The variances at the surface are parameterized in a similar fashion for all these three quantities as:

$$\sigma_w = 1.34 w_* \left(\frac{z_0}{z_{top}}\right)^{1/3}\left(1 - 0.8\frac{z_0}{z_{top}}\right), \tag{A8}$$

$$\sigma_{q_t} = 1.34 q_* \left(\frac{z_0}{z_{top}}\right)^{-1/3}, \tag{A9}$$

and

$$\sigma_{\theta_v} = 1.34 \theta_* \left(\frac{z_0}{z_{top}}\right)^{-1/3}, \tag{A10}$$

with z_{top} being the depth of the convective layer and $w_* \equiv \left(\frac{g}{\bar{\theta}_v}\overline{w'\theta'_v}|_s z_{top}\right)$ being a convective velocity similar to the Deardorff convective velocity. Here we take $z_0 = 50$ m, and $q_* = \frac{\overline{w'q'_t}|_s}{w_*}$ and $\theta_* = \frac{\overline{w'\theta'_v}|_s}{w_*}$ are the convective moisture and temperature scales.

Acknowledgments
This work was supported by the Caltech President's and Director's Fund program. The source code for the model used in this study, the WRF V 3.5.1, is freely available at http://www2.mmm.ucar.edu/wrf/users/download/. The input files necessary to reproduce the experiments with WRF as well as the relevant model output are available from the corresponding author upon request (ritthikiit@gmail.com). Part of this research was carried out at the Jet Propulsion Laboratory, California Institute of Technology, under a contract with the National Aeronautics and Space Administration. Part of this research was supported by the U.S. Department of Energy, Office of Biological and Environmental Research, Earth System Modeling. We also acknowledge the support provided by the Office of Naval Research, Marine Meteorology Program, the NASA MAP Program, and the NOAA/CPO MAPP Program.

A2. Entrainment Rate

Entrainment (ε) into an updraft is assumed to be the result of a stochastic discrete process. For an updraft that travels a distance δz, the probability that an entrainment event occurs is assumed to follow the Binomial distribution. This probability as well as the strength of the entrainment rate are both height independent. This implies that the actual number of entrainment events for the updraft traveling over a finite distance Δz (which is the distance between two vertical model levels) follows the Poisson distribution (denoted here by $\mathcal{P}$). Mathematically:

$$\varepsilon(\Delta z) = \frac{\varepsilon_0}{\Delta z}\mathcal{P}\left(\frac{\Delta z}{L_\varepsilon}\right), \tag{A11}$$

where $\varepsilon(\Delta z)$ represents the mean entrainment rate over the height of Δz, L_ε represents the length scale the updraft needs to travel to entrain once; here we assume $L_\varepsilon = 100$ m. The value of ε_0 is taken to be 0.1. This formulation is similar to the one in Suselj et al. (2013) except for the simplification of the value of L_ε.

References

Bengtsson, L., Hodges, K. L., & Hagemann, S. (2004). Sensitivity of the ERA40 reanalysis to the observing system: Determination of the global atmospheric circulation from reduced observations. *Tellus, Series A*, *56*, 456–471. https://doi.org/10.1111/j.1600-0870.2004.00079.x

Bhattacharya, R., Bordoni, S., & Teixeira, J. (2017). Tropical precipitation extremes: Response to SST-induced warming in aquaplanet simulations. *Geophysical Research Letters*, *44*, 3374–3383. https://doi.org/10.1002/2017GL073121

Biswas, M. K., Bernardet, L., & Dudhia, J. (2014). Sensitivity of hurricane forecasts to cumulus parameterizations in the HWRF model. *Geophysical Research Letters*, *41*, 9113–9119. https://doi.org/10.1002/2014GL062071

Broginez, H., & Pierrehumbert, R. T. (2007). Intercomparison of tropical tropospheric humidity in GCMs with AMSU-B water vapor data. *Geophysical Research Letters*, *34*, L17812. https://doi.org/10.1029/2006GL029118

Cavallo, S. M., Brener, J., & Snyder, C. (2016). Diagnosing model errors from time-averaged tendencies in the Weather Research and Forecasting (WRF) model. *Monthly Weather Review*, *144*, 759–779. https://doi.org/10.1175/MWR-D-15-0120.1

Cesana, G., Suselj, K., & Brient, F. (2017). On the dependence of cloud feedbacks on physical parameterizations in WRF aquaplanet simulations. *Geophysical Research Letters*, *44*, 10762–10771. https://doi.org/10.1002/2017GL074820

Cheinet, S. (2003). A multiple mass-flux parameterization for the surface-generated convection. Part I: Dry plumes. *Journal of the Atmospheric Sciences*, *60*(18), 2313–2327. https://doi.org/10.1175/1520-0469

Chikhar, K., & Gauthier, P. (2015). On the effect of boundary conditions on the Canadian Regional Climate Model: Use of process tendencies. *Climate Dynamics*, *45*, 2515–2526. https://doi.org/10.1007/s00382-015-2488-2

Collins, W. D., Rasch, P. J., Boville, B. A., Hack, J. J., McCaa, J. R., Williamson, D. L., et al. (2006). The formulation and atmospheric simulation of the Community Atmosphere Model Version 3 (CAM3). *Journal of Climate*, *19*, 2144–2161. https://doi.org/10.1175/JCLI3760.1

Del Genio, A. D., Lacis, A. A., & Ruedy, R. A. (1991). Simulations of the effect of a warmer climate on atmospheric humidity. *Nature*, *351*, 382–385. https://doi.org/10.1038/351382a0

de Roode, S. R., Siebesma, A. P., Jonker, H. J. J., & de Voogd, Y. (2012). Parameterization of the vertical velocity equation for shallow cumulus clouds. *Monthly Weather Review*, *140*(8), 2424–2436. https://doi.org/10.1175/MWR-D-11-00277.1

Dudhia, J. (1989). Numerical study of convection observed during the winter monsoon experiment using a mesoscale two-dimensional model. *Journal of the Atmospheric Sciences*, *46*(20), 3077–3107. https://doi.org/10.1175/1520-0469(1989)046<3077:NSOCOD>2.0.CO;2

Dudhia, J., Wang, W., & Chen, M. (2012). Convective parameterization options in wrf v3.4. In *University Corporation for Atmospheric Research (UCAR): 13 th Annual Weather Research and Forecasting (WRF) model user's workshop*. Retrieved from http://www2.mmm.ucar.edu/wrf/users/workshops/WS2012/ppts/lecture4.pdf; http://www2.mmm.ucar.edu/wrf/users/workshops/WS2012/WorkshopPapers.php

Emmanuel, K., Neelin, J., & Bretherton, C. S. (1994). On large-scale circulations in convecting atmospheres. *Quarterly Journal of the Royal Meteorological Society*, *120*, 1111–1143. https://doi.org/10.1002/qj.49712051902

Feldl, N., & Bordoni, S. (2016). Characterizing the Hadley circulation response through regional climate feedbacks. *Journal of Climate*, *29*, 613–622. https://doi.org/10.1175/JCLI-D-15-0424.1

Han, J., & Pan, H.-L. (2011). Revision of convection and vertical diffusion schemes in the NCEP Global Forecast System. *Weather and Forecasting*, *26*, 520–533. https://doi.org/10.1175/WAF-D-10-05038.1

Held, I. (2000). The general circulation of the atmosphere. In *Proceedings of the geophysical fluid dynamics program, Woods Hole, MA* (pp. 1–70). Geophysical Fluid Dynamics Laboratory, lecture at Woods Hole Oceanographic Institution. Retrieved from http://gfdl.noaa.gov/cms-filesystem-action/user_files/ih/lectures/woods_hole.pdf; https://www.whoi.edu/page.do?pid=13076

Held, I., & Hou, A. (1980). Nonlinear axially symmetric circulations in a nearly inviscid atmosphere. *Journal of the Atmospheric Sciences*, *37*, 515–533.

Hoskins, B., Neale, R., Rodwell, M., & Yang, G. Y. (1999). Aspects of the large scale tropical atmospheric circulation. *Tellus, Series A*, 33–44. https://doi.org/10.1034/j.1600-0889.1999.00004.x

Khouider, B., Majda, A. J., & Stechmann, S. N. (2013). Climate science in the tropics: Waves, vortices and PDEs. *Nonlinearity*, *26*, R1–R68. https://doi.org/10.1088/0951-7715/26/1/R1

Knutson, T. R., & Manabe, S. (1995). Time-mean response over the tropical Pacific to increased CO_2 in a coupled ocean-atmosphere model. *Journal of Climate*, *8*, 2181–2199.

Mapes, B. E. (1997). Equilibrium vs. activation control of large-scale variations of tropical deep convection. *The Physics and Parameterization of Moist Atmospheric Convection*, *505*, 321–348. https://doi.org/10.1007/978-94-015-8828-7_13

Medeiros, B., Stevens, B., & Bony, S. (2015). Using aquaplanets to understand the robust responses of comprehensive climate models to forcing. *Climate Dynamics*, *44*, 1957–1977. https://doi.org/10.1007/s00382-014-2138-0

Medeiros, B., Stevens, B., Held, I. M., Zhao, M., Williamson, D. L., Olson, J. G., et al. (2008). Aquaplanets, climate sensitivity, and low clouds. *Journal of Climate*, *21*(19), 4974–4991. https://doi.org/10.1175/2008JCLI1995.1

Medeiros, B., Williamson, D. L., & Olson, J. G. (2016). Reference aquaplanet climate in the Community Atmosphere Model, version 5. *Journal of Advances in Modeling Earth Systems*, *8*, 406–424. https://doi.org/10.1002/2015MS000593

Mlawer, E. J., Taubman, S. J., Brown, P. D., Iacono, M. J., & Clough, S. A. (1997). Radiative transfer for inhomogeneous atmospheres: RRTM, a validated correlated-k model for the longwave. *Journal of Geophysical Research*, *102*(D14), 16,663. https://doi.org/10.1029/97JD00237

Moebis, B., & Stevens, B. (2012). Factors controlling the position of the Intertropical Convergence Zone on an aquaplanet. *Journal for Advances in Modeling Earth Systems*, *4*, M00A04. https://doi.org/10.1029/2012MS000199

Morrison, H., Thompson, G., & Tatarskii, V. (2009). Impact of cloud microphysics on the development of trailing stratiform precipitation in a simulated squall line: Comparison of one- and two-moment schemes. *Monthly Weather Review*, *137*(3), 991–1007. https://doi.org/10.1175/2008MWR2556.1

Nakanishi, M., & Niino, H. (2006). An improved Mellor-Yamada level-3 model: Its numerical stability and application to a regional prediction of advection fog. *Boundary-Layer Meteorology*, *119*(2), 397–407. https://doi.org/10.1007/s10546-005-9030-8

Neelin, J., & Held, I. (1987). Modeling tropical convergence based on moist static energy budget. *Monthly Weather Review*, *115*, 3–12. https://doi.org/10.1175/1520-0493(1987)115<003:MTCBOT>2.0.CO;2

Numaguti, A. (1993). Dynamics and energy balance of the Hadley circulation and the tropical precipitation zones: Significance of the distribution of evaporation. *Journal of the Atmospheric Sciences*, *13*, 1874–1887. https://doi.org/10.1175/1520-0469(1993)050,1874:DAEBOT.2.0.CO;2

O'Gorman, P. A., Allan, R. P., Byrne, M. P., & Previdi, M. (2012). Energetic constraints on precipitation under climate change. *Surveys in Geophysics*, *33*, 585–608. https://doi.org/10.1007/s10712-011-9159-6

Pan, H.-L., & Wu, W.-S. (1995). *Implementing a mass flux convective parameterization package for the NMC medium-range forecast model* (Office Note 409). Silver Spring, MD: U.S. Department of Commerce, National Oceanic and Atmospheric Administration.

Park, S., & Bretherton, C. S. (2009). The University of Washington Shallow Convection and Moist Turbulence Schemes and their impact on climate simulations with the Community Atmosphere Model. *Journal of Climate*, *22*, 3449–3469. https://doi.org/10.1175/2008JCLI2557.1

Pauluis, O., Czaja, A., & Korty, R. (2010). The global atmospheric circulation in moist isentropic coordinates. *Journal of Climate*, *23*, 3077–3093.

Pierrehumbert, R. T. (1998). Lateral mixing as a source of subtropical water vapor. *Geophysical Research Letters*, *25*(2), 151–154. https://doi.org/10.1029/97GL03563

Pierrehumbert, R. T. (2002). The hydrologic cycle in deep-time climate problems. *Nature*, *419*, 191–198. https://doi.org/10.1038/nature01088

Pierrehumbert, R. T., Brogniez, H., & Roca, R. (2007). On the relative humidity of the atmosphere. In T. Schneider & A. Sobel (Eds.), *The global circulation of the atmosphere*. Princeton, NJ: Princeton University Press.

Prive, N., & Plumb, R. (2007). Monsoon dynamics with interactive forcing. Part I: Axisymmetric studies. *Journal of the Atmospheric Sciences*, *64*, 1417–1430. https://doi.org/10.1175/JAS3916.1

Raymond, D. J. (1995). Regulation of moist convection over the west Pacific warm pool. *Journal of the Atmospheric Sciences*, *52*(22), 3945–3959. https://doi.org/10.1175/1520-0469(1995)052<3945:ROMCOT>2.0.CO;2

Raymond, D. J., Sessions, S., Sobel, A., & Fuchs, Z. (2009). The mechanics of gross moist stability. *Journal of Advances in Modeling Earth Systems*, *1*, 9. https://doi.org/10.3894/JAMES.2009.1.9

Richter, J. H., & Rasch, P. J. (2008). Effects of convective momentum transport on the atmospheric circulation in the Community Atmosphere Model, Version 3. *Journal of Climate*, *21*, 1487–1499. https://doi.org/10.1175/2007JCLI1789.1

Seo, K.-H., Frierson, D., & Son, J.-H. (2014). A mechanism for future changes in Hadley circulation strength in CMIP5 climate change simulations. *Geophysical Research Letters*, *40*, 5251–5258. https://doi.org/10.1002/2014GL060868

Siebesma, A. P., Soares, P. M. M., & Teixeira, J. (2007). A combined eddy-diffusivity mass-flux scheme for the convective boundary layer. *Journal of the Atmospheric Sciences*, *64*, 1230–1248. https://doi.org/10.1175/JAS3888.1

Skamarock, W., Klemp, J., Dudhia, J., Gill, D., Barker, D., Duda, M., et al. (2008). *A description of the advanced research WRF Version 3* (NCAR Technical Note NCAR/TN-468+STR). Boulder, CO: National Center for Atmospheric Research. https://doi.org/10.5065/D6DZ069T

Spencer, A., Ming, Y., & Held, I. M. (2015). Mechanisms of forced tropical meridional energy flux change. *Journal of Climate*, *28*, 1725–1742. https://doi.org/10.1175/JCLI-D-14-00165.1

Stevens, B., & Bony, S. (2013). What are climate models missing? *Science*, *340*, 1053–1054. https://doi.org/10.1126/science.1237554

Suselj, K., Hogan, T. F., & Teixeira, J. (2014). Implementation of a stochastic eddy-diffusivity/mass-flux parameterization into the Navy Global Environmental Model. *Weather and Forecasting*, *29*(6), 1374–1390. https://doi.org/10.1175/WAF-D-14-00043.1

Suselj, K., Teixeira, J., & Chung, D. (2013). A unified model for moist convective boundary layers based on a stochastic eddy-diffusivity/mass-flux parameterization. *Journal of the Atmospheric Sciences*, *70*(7), 1929–1953. https://doi.org/10.1175/JAS-D-12-0106.1

Suselj, K., Teixeira, J., & Matheou, G. (2012). Eddy diffusivity/mass flux and shallow cumulus boundary layer: An updraft PDF multiple mass flux scheme. *Journal of the Atmospheric Sciences*, *69*(5), 1513–1533. https://doi.org/10.1175/JAS-D-11-090.1

Tiedtke, M. (1989). A comprehensive mass flux scheme for cumulus parameterization in large-scale models. *Monthly Weather Review*, *117*, 1779–1800. https://doi.org/10.1175/1520-0493(1989)117<1779:ACMFSF>2.0.CO;2

Trenberth, K., Dai, A., Rasmussen, R., & Parsons, D. (2003). The changing character of precipitation. *Bulletin of the American Meteorological Society*, *84*, 1205–1217. https://doi.org/10.1175/BAMS-84-9-1205

Voigt, A., & Shaw, T. A. (2015). Circulation response to warming shaped by radiative changes of clouds and water vapour. *Nature Geoscience*, *8*, 102–106. https://doi.org/10.1038/ngeo2345

Williams, K. D., & Brooks, M. (2008). Initial tendencies of cloud regimes in the Met Office unified model. *Journal of Climate*, *21*, 833–840. https://doi.org/10.1175/2007JCLI1900.1

Williamson, D., Blackburn, M., Hoskins, B. J., Nakajima, K., Ohfuchi, W., Takahashi, Y. O., et al. (2012). *APE atlas* (NCAR Technical Note NCAR/TN-484+STR). Boulder, CO: National Center for Atmospheric Research. https://doi.org/10.5065/D6FF3QBR

Zhang, C., Wang, Y., & Hamilton, K. (2011). Improved representation of boundary layer clouds over the southeast Pacific in ARW-WRF using a modified Tiedtke cumulus parameterization scheme. *Monthly Weather Review*, *139*(11), 3489–3513. https://doi.org/10.1175/MWR-D-10-05091.1

Zhang, D.-L., & Zheng, W.-Z. (2004). Diurnal cycles of surface winds and temperatures as simulated by five boundary layer parameterizations. *Journal of Applied Meteorology*, *43*, 157–169. https://doi.org/10.1175/1520-0450